

MARA: Continuous SE(3)-Equivariant Attention for Molecular Force Fields

Francesco Leonardi¹ Boris Bonev² Kaspar Riesen¹

Abstract

Machine learning force fields (MLFFs) have become essential for accurate and efficient atomistic modeling. Despite their high accuracy, most existing approaches rely on fixed angular expansions, limiting flexibility in weighting local geometric interactions. We introduce Modular Angular-Radial Attention (MARA), a module that extends spherical attention – originally developed for SO(3) tasks – to the molecular domain and SE(3), providing an efficient approximation of equivariant interactions. MARA operates directly on the angular and radial coordinates of neighboring atoms, enabling flexible, geometrically informed, and modular weighting of local environments. Unlike existing attention mechanisms in SE(3)-equivariant architectures, MARA can be integrated in a plug-and-play manner into models such as MACE without architectural modifications. Across molecular benchmarks, MARA improves energy and force predictions, reduces high-error events, and enhances robustness. These results demonstrate that continuous spherical attention is an effective and generalizable geometric operator that increases the expressiveness, stability, and reliability of atomistic models.

1. Introduction

Machine Learning Force Fields (MLFFs) have become a central tool for atomistic simulations in chemistry and materials science (Botu et al., 2017; Unke et al., 2021), offering an effective compromise between the accuracy of *ab initio* electronic structure methods, such as Density Functional Theory (DFT), and the computational efficiency required for large-scale simulations (Cheng et al., 2020; Chmiela et al., 2023). Although early MLFF approaches included neural networks (Behler & Parrinello, 2007) or fixed parametric

¹Institute of Computer Science, University of Bern, 3012 Bern, Switzerland ²NVIDIA Corporation, 95051 Santa Clara, CA, USA. Correspondence to: Francesco Leonardi <francesco.leonardi@unibe.ch>.

forms (Thompson et al., 2015; Shapeev, 2016), recent advances leverage SE(3)-equivariant graph neural networks to encode physical symmetries and capture complex geometric interactions (Bronstein et al., 2021). Models such as NequIP (Batzner et al., 2021) and MACE (Batazia et al., 2022b) trained on high-quality quantum datasets, achieve near-DFT accuracy and the scalability required for larger systems and longer simulations (Behler, 2016; Chmiela et al., 2018).

Despite their expressivity, most SE(3)-equivariant model angular dependencies using fixed basis expansions or discrete neighbor sets, limiting flexibility in weighting continuous directional contributions (Batzner et al., 2021). Inspired by the success of attention mechanisms (Vaswani et al., 2017) in other domains, recent work has proposed SE(3)-equivariant Transformers (Liao & Smidt, 2023; Liao et al., 2024), but these typically operate over discrete atomic neighborhoods rather than the continuous spatial domain.

A complementary approach leverages attention directly on the sphere, providing efficient approximations to SO(3)-equivariant operators and enabling flexible modeling of angular dependencies without relying on high-order tensor products (Bonev et al., 2025). Such spherical attention mechanisms have achieved strong results in geometric tasks, including spherical image segmentation and physical simulations (Cho et al., 2022; Benny & Wolf, 2025; Bonev et al., 2025). Despite their advantages, they have not been explored in the context of atomistic modeling. In particular, it is unclear how these approaches can be extended to approximate SE(3) equivariance – requiring the joint treatment of angular and radial degrees of freedom – or how they can be integrated into existing MLFF architectures without compromising computational efficiency.

Our contributions In this work, we introduce a continuous spherical attention mechanism that operates directly on local atomic environments and provides an efficient approximation to SE(3)-equivariance. Our approach reformulates attention as an operator over directions and distances, using a structured spherical discretization that naturally separates angular and radial dependencies. This formulation enables flexible, geometry-aware weighting of local atomic environments. Moreover, we demonstrate a plug-and-play integration of this module into existing SE(3)-equivariant

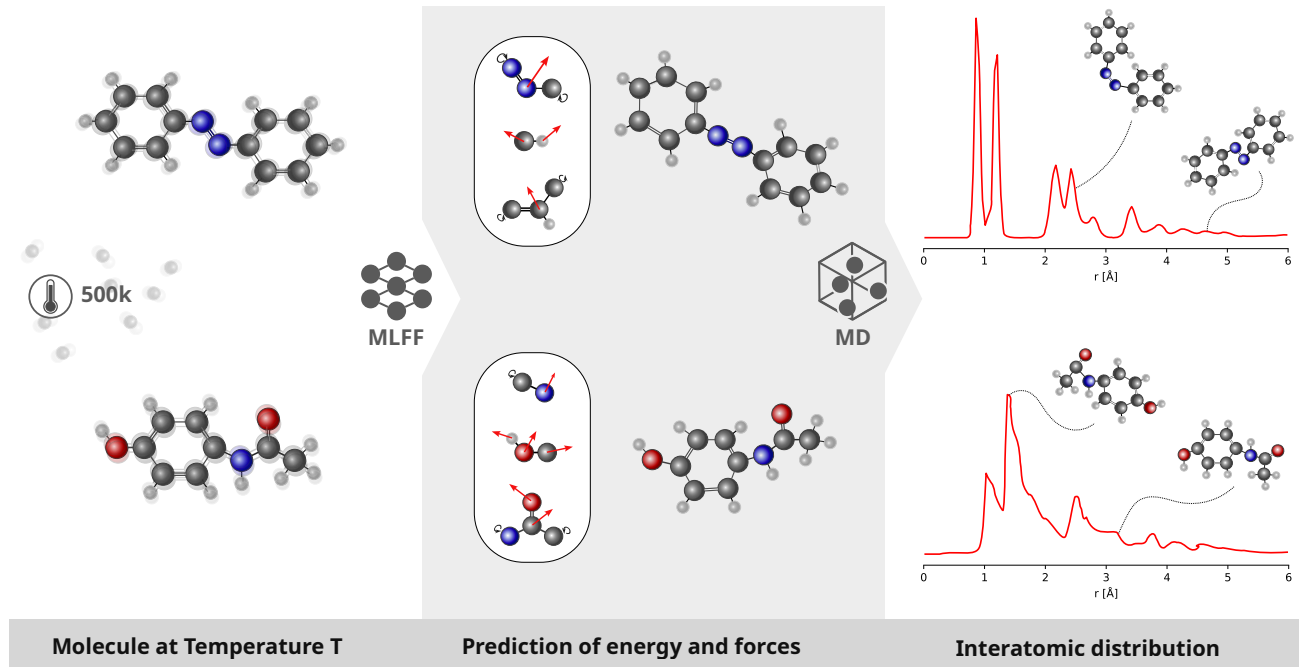


Figure 1. Illustration of a Machine Learning Force Field (MLFF) modeled with Equivariant Graph Neural Networks (EGNNs). Given a molecular configuration at a specific temperature, the model predicts the forces acting on each atom, which are then used to estimate the molecule’s subsequent configuration. Molecular configurations that occur more frequently are captured more accurately by the model, while less frequent configurations, which can be visualized through the interatomic distribution, are inherently more uncertain.

MLFFs, instantiated in MACE to validate its integration, while remaining fully compatible with SE(3)-equivariant message passing. Finally, we evaluate the effectiveness of our approach on representative molecular benchmarks, showing consistent improvements over current baselines with a controlled computational overhead.

2. Related Work

Equivariant graph neural networks for MLFFs. Early MLFFs relied on neural networks (Behler, 2016) or fixed parametric forms (Bartók et al., 2010; Thompson et al., 2015; Shapeev, 2016), achieving moderate accuracy and scalability. Graph-based models such as SchNet (Schütt et al., 2017) and DimeNet (Klicpera et al., 2020) are invariant to translations, rotations, and atom permutations. More recent approaches explicitly enforce SE(3) equivariance (Bronstein et al., 2021; Duval et al., 2023). These include Tensor Field Network (TFN)-based architectures (Thomas et al., 2018) as well as other SE(3)-equivariant graph neural networks, such as the E(n)-equivariant GNN (Satorras et al., 2021). Prominent SE(3)-equivariant message-passing models include NequIP (Batzner et al., 2021), Allegro (Musaelian et al., 2022), BOTNet (Batatia et al., 2022a), MACE (Batatia et al., 2022b), UNiTE (Qiao et al., 2022), QuinNet (Wang et al.,

2023a), and VisNet (Wang et al., 2024), which leverage equivariant message passing and higher-order geometric representations to achieve strong performance across molecular and materials benchmarks. While highly expressive, many of these architectures rely on fixed angular basis expansions or predefined correlation orders, which can increase model complexity when modeling flexible angular interactions.

Transformer-based approaches in MLFFs. Motivated by the success of attention-based models in other domains (Vaswani et al., 2017), several works have introduced SE(3)-equivariant Transformer architectures, including the SE(3)-Transformer (Fuchs et al., 2020), Equiformer (Liao & Smidt, 2023), EquiformerV2 (Liao et al., 2024), and SO3krates (Frank et al., 2024). These models apply attention mechanisms over local atomic neighborhoods while preserving equivariance through tensor representations and spherical harmonics. Attention is defined over discrete sets of neighboring atoms, with angular dependencies handled explicitly via spherical-harmonic-based equivariant features, rather than through attention operators acting continuously over the angular domain. In contrast, Equivariant Spherical Transformer (An et al., 2025) applies a Transformer-like architecture in the spherical Fourier domain aiming approximate equivariance via uniform spherical sampling.

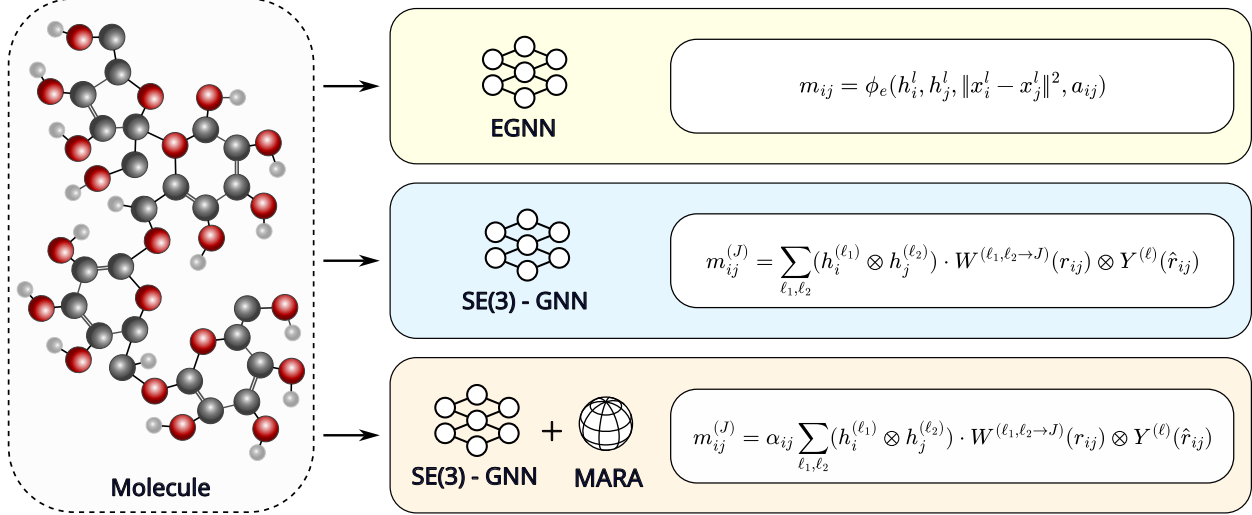


Figure 2. The molecule is represented as a 3D molecular graph, in which the nodes are characterized by scalar features and spatial coordinates. Different equivariant graph neural networks process this information using different message passing mechanisms: Equivariant Graph Neural Networks (EGNN), SE(3)-equivariant networks (SE(3)-GNN), and SE(3)-GNN enriched with MARA.

Spherical attention mechanisms. Recent work has explored attention mechanisms defined directly on the sphere (Bonev et al., 2025). Such spherical Transformers have demonstrated strong performance in geometric tasks, including simulations of shallow water equations and spherical image segmentation (Bonev et al., 2025). By operating on spherical signals, these methods provide an efficient way to model angular dependencies and to construct operators with rotational equivariance, without explicitly relying on high-order irreducible tensor representations. To our knowledge, attention on the sphere has not yet been applied to atomistic modeling, providing an opportunity to extend these ideas to SE(3)-equivariant MLFFs, which we explore in this work.

3. Method

Graph representation. A molecule is represented as a graph $G = (V, E)$, where $V = \{1, \dots, N\}$ denotes the set of nodes corresponding to atoms, and $E \subseteq V \times V$ denotes the set of edges encoding pairwise interactions, such as chemical bonds or neighborhood relations. Each node $i \in V$ is associated with a feature vector $\mathbf{h}_i \in \mathbb{R}^{d_h}$, while each edge $(i, j) \in E$ may be associated with an edge feature vector $\mathbf{e}_{ij} \in \mathbb{R}^{d_e}$. Edge features may encode bond types, interatomic distances, or other geometric descriptors.

3D molecular graphs. In addition to node and edge features, each node $i \in V$ is associated with a three-dimensional coordinate $\mathbf{x}_i \in \mathbb{R}^3$, representing the atomic position in Euclidean space. Edges are typically defined either by spatial proximity, e.g., connecting nodes within a cutoff radius $r > 0$.

Geometric symmetries. Molecular systems are equivariant to rigid motions in three-dimensional space. We consider the action of the special Euclidean group $SE(3)$ on the atomic coordinates, such that for any $(R, \mathbf{t}) \in SE(3)$,

$$\mathbf{x}_i \mapsto R\mathbf{x}_i + \mathbf{t}. \quad (1)$$

Node and edge features are assumed to transform as scalars under $SE(3)$, and therefore remain invariant. Models operating on 3D molecular graphs should preserve $SE(3)$ -equivariance for vectorial quantities (such as forces), with invariance enforced at the output level for scalar target properties, such as energies or molecular descriptors.

Attention on the sphere. We base our method on the continuous-domain attention mechanism, which can be understood as a generalized kernel regression over query, key, and value signals. For inputs $q, k : S^2 \rightarrow \mathbb{R}^d$ and $v : S^2 \rightarrow \mathbb{R}^e$, the spherical attention operator is defined as

$$\begin{aligned} \text{Attn}_{S^2}[q, k, v](x) \\ = \frac{\int_{S^2} \exp(q(x)^\top k(x')/\sqrt{d}) v(x') d\mu(x')}{\int_{S^2} \exp(q(x)^\top k(x')/\sqrt{d}) d\mu(x')}, \end{aligned} \quad (2)$$

where μ denotes the invariant Haar measure on the sphere. This construction ensures that the attention is equivariant under 3D rotations $R \in SO(3)$:

$$\text{Attn}_{S^2}[q, k, v](R^{-1}x) = \text{Attn}_{S^2}[q', k', v'](x). \quad (3)$$

To implement the operator numerically, Bonev et al. (2025) discretize the spherical domain using a set of grid points

$\{g_k \in S^2\}_{k=1}^{N_{\text{grid}}}$ and associated quadrature weights ω_i , such that

$$\int_{S^2} u(x) d\mu(x) \approx \sum_{k=1}^{N_{\text{grid}}} u(g_k) \omega_k. \quad (4)$$

This yields a discrete attention mechanism that preserves approximate SO(3) equivariance, enabling consistent evaluation under 3D rotations.

Attention SE(3)-equivariant approximation for molecular graphs. While the spherical attention operator is approximately equivariant under rotations SO(3), molecular coordinates also undergo translations in \mathbb{R}^3 . To capture both directional and distance-dependent interactions, we associate with each atom $i \in V$ a discrete spherical grid $\{g_k \in S^2\}_{k=1}^{N_{\text{grid}}}$ and define a scalar field $f_k : S^2 \rightarrow \mathbb{R}$, discretized on the spherical grid, encoding the Euclidean distances to its neighboring atoms $j \in \mathcal{N}(i)$. Concretely, for each neighbor j , we set

$$f_{jk}(g_k) = \|\mathbf{x}_j - (\mathbf{x}_i + r_{jk} g_k)\| \quad (5)$$

where $r_{jk} = \|\mathbf{x}_j - \mathbf{x}_i\|$ and $g_k \in S^2$ (unit vectors). This construction guarantees that the scalar field attains its minimum along the direction pointing to each neighboring atom. Unlike models such as SchNet (Schütt et al., 2017), which rely solely on interatomic distances, our spherical scalar field encodes both directional and distance information, enabling the network to distinguish geometrically distinct configurations.

Spherical positional embeddings. Following the idea of the original work (Bonev et al., 2025), we associate each point of the spherical grid g_k with a learnable positional embedding p_k .

Atom-centered queries, keys, and values are obtained via separate linear projections of the node features, the spherical scalar field, and the positional embeddings, which are then summed:

$$\begin{aligned} \mathbf{q}_{i,j,k} &= W_h \mathbf{h}_i + W_f f_{jk}(g_k) + p_k, \\ \mathbf{k}_{i,j,k} &= W'_h \mathbf{h}_j + W'_f f_{jk}(g_k) + p_k, \\ \mathbf{v}_{i,j,k} &= W''_h \mathbf{h}_j + W''_f f_{jk}(g_k) + p_k. \end{aligned}$$

where $W_h, W'_h, W''_h \in \mathbb{R}^{d \times d_h}$ and $W_f, W'_f, W''_f \in \mathbb{R}^{d \times d_f}$ are learnable linear mappings. For simplicity, we choose the value dimension to coincide with the query/key dimension, i.e. $e = d$. This approach mirrors standard Transformer positional embeddings, allowing the attention to be aware of spherical directions while maintaining approximate rotation equivariance in the spherical domain and translation invariance through relative distances.

Integration into SE(3)-equivariant message passing.

The spherical attention module is integrated as a scalar interaction block within existing SE(3)-equivariant architectures. In particular, we apply it in parallel to the standard equivariant message passing layers of MACE (Batatia et al., 2022b). The choice of MACE is motivated by its widespread adoption in the current state of the art of machine learning force fields, where its architecture serves as the backbone for several foundation models (Batatia et al., 2025). In standard SE(3)-equivariant models such as MACE, atom i updates its features by aggregating messages from neighbors $j \in \mathcal{N}(i)$:

$$\tilde{m}_{i,j}^{(J)} = \sum_{\ell_1, \ell_2} (h_i^{(\ell_1)} \otimes h_j^{(\ell_2)}) \cdot W^{(\ell_1, \ell_2 \rightarrow J)}(r_{ij}) \otimes Y^{(\ell)}(\hat{r}_{ij}), \quad (6)$$

where $W^{(\ell_1, \ell_2 \rightarrow J)}$ combines radial functions, spherical harmonics, and Clebsch–Gordan coefficients.

At each interaction layer, the backbone computes equivariant messages $\tilde{m}_{i,j,J}^{(t)}$ using tensor products of irreducible representations. The gating coefficient α_{ij} is obtained from the output of the spherical attention operator by applying a readout over channels and spherical grid points:

$$\alpha_{ij} = \sigma\left(W_{\text{gate}} \text{Pool}_{k,c} [\text{Attn}_{S^2}[\mathbf{q}_{i,j,k}, \mathbf{k}_{i,j,k}, \mathbf{v}_{i,j,k}](g_k)]\right) \quad (7)$$

where $\text{Pool}_{k,c}$ indicates a rotation-invariant pooling over spherical directions k and attention feature channels c . The final message update is then given by

$$m_{i,J}^{(t)} = \sum_{j \in \mathcal{N}(i)} \alpha_{ij} \tilde{m}_{i,j,J}^{(t)}. \quad (8)$$

Since α_{ij} is a scalar, equivariance is preserved only if α_{ij} is invariant with respect to rotations and translations. Due to the discrete approximation of the continuous attention mechanism, the resulting operation is only approximately SE(3)-equivariant.

This formulation enables direction-dependent weighting of local atomic environments while remaining fully compatible with existing equivariant message passing schemes. When $\alpha_{ij} = 1$, the formulation reduces exactly to the original MACE update, highlighting the plug-and-play nature of the proposed module.

Thus, by combining the scalar spherical attention module with the MACE backbone, we obtain an enhanced approximately SE(3)-equivariant message passing architecture, which we refer to as MACE-MARA

4. Experiments

Dataset We evaluate the proposed method on two established benchmarks for machine learning force fields: revised

Table 1. Performance on the rMD17 dataset. Results are reported in terms of mean absolute error (MAE). Energies (E) and forces (F) are measured in kcal/mol and kcal/mol/Å, respectively. The best results are highlighted in bold, while the second-best results are underlined. Results of the models are taken from Wang et al. (2023a).

MOLECULE		MACE								
		UNiTE	NEQUIP	ALLEGRO	BOTNET	ViSNET	QUINNET	BASELINE	MARA	Δ (%)
ASPIRIN	E	0.055	0.0530	0.0507	0.0530	<u>0.0445</u>	0.0486	0.0507	0.0419	-17.36
	F	0.175	0.1891	0.1684	0.1960	<u>0.1520</u>	<u>0.1429</u>	0.1522	0.1413	-7.15
AZOBENZENE	E	0.025	0.0161	0.0277	<u>0.0161</u>	0.0156	0.0394	0.0277	0.0185	-33.21
	F	0.097	0.0669	0.0600	<u>0.0761</u>	<u>0.0585</u>	0.0513	0.0692	0.0653	-5.59
BENZENE	E	0.002	<u>0.0009</u>	0.0069	0.0007	0.0007	0.0096	0.0092	0.0048	-47.83
	F	0.017	<u>0.0069</u>	0.0046	0.0069	0.0056	<u>0.0047</u>	0.0069	0.0064	-7.25
ETHANOL	E	0.014	0.0092	0.0092	0.0092	0.0078	0.0096	<u>0.0032</u>	0.0026	-18.75
	F	0.085	0.0646	<u>0.0484</u>	0.0738	0.0522	0.0516	<u>0.0484</u>	0.0459	-5.17
MALONALDEHYDE	E	0.025	0.0184	0.0138	0.0185	<u>0.0132</u>	0.0168	0.0185	0.0091	-50.81
	F	0.152	0.1176	0.0830	0.1338	0.0893	<u>0.0875</u>	0.0946	0.0896	-5.29
NAPHTHALENE	E	0.011	0.0046	0.0046	0.0046	<u>0.0057</u>	0.0174	0.0115	0.0142	+23.48
	F	0.060	0.0300	0.0208	0.0415	0.0291	<u>0.0242</u>	0.0369	0.0357	-3.25
PARACETAMOL	E	0.044	0.0323	0.0346	0.0300	0.0258	0.0362	0.0300	<u>0.0264</u>	-12.00
	F	0.164	0.1361	0.1130	0.1338	<u>0.1029</u>	0.0979	0.1107	0.1054	-4.76
SALICYLICACID	E	0.017	0.0161	0.0208	0.0285	<u>0.0161</u>	0.0330	0.0208	0.0248	+19.23
	F	0.088	0.0922	<u>0.0669</u>	0.0992	<u>0.0795</u>	0.0771	0.0715	0.0645	-9.79
TOLUENE	E	0.010	0.0069	0.0092	<u>0.0069</u>	0.0059	0.0139	0.0115	0.0158	+37.39
	F	0.058	0.0369	0.0415	<u>0.0438</u>	<u>0.0264</u>	0.0244	0.0350	0.0325	-7.14
URACIL	E	0.013	0.0092	0.0138	<u>0.0092</u>	0.0069	0.0149	0.0115	0.0146	+26.96
	F	0.088	0.0669	0.0415	0.0738	0.0495	0.0487	0.0484	<u>0.0460</u>	-4.96
AVERAGE	E	0.022	0.0175	0.0191	0.0177	0.0142	0.0239	0.0195	<u>0.0173</u>	-11.28
	F	0.098	0.0807	0.0648	0.0879	0.0645	0.0610	0.0674	<u>0.0633</u>	-6.06

MD17 (rMD17) (Christensen & von Lilienfeld, 2020) and MD22 (Chmiela et al., 2023). The rMD17 dataset is a reimplementation of MD17 (Chmiela et al., 2017), which resolves numerical inconsistencies in the original benchmark with higher accuracy. In contrast, MD22 includes larger and more flexible molecules, resulting in more complex potential energy surfaces.

Both datasets consist of *ab initio* molecular dynamics trajectories of organic molecules and provide standardized benchmarks for the development and evaluation of machine learning models of molecular potential energy surfaces. Model performance is reported in terms of mean absolute error (MAE) for both energies (kcal/mol) and forces (kcal/mol/Å).

Training We train the MACE baseline in the high-dimensional configuration and following exactly the training protocol described in the original work (Batatia et al., 2022a;b). We retrain the MACE-MARA in the same deterministic environment and identical settings, ensuring that any observed performance differences are solely attributable to the proposed module.

The attention module is implemented as a sinusoidal gating mechanism to modulate the contribution of neighboring atoms based on their positions. We employ the same hyperparameters across all molecules: a 4×8 grid corresponding

to 32 equiangular sampling points, single-head attention, and no attention dropout. All experiments are implemented in PyTorch and trained on an NVIDIA H100 GPU.

4.1. Results

Table 1 shows the MAEs on the rMD17 benchmark, comparing our MACE-MARA to several state-of-the-art models, including NequIP (Batzner et al., 2021), MACE (Batatia et al., 2022b), Allegro (Musaelian et al., 2022), BOTNet (Batatia et al., 2022a), UNiTE (Qiao et al., 2022), QuinNet (Wang et al., 2023a), and ViSNet (Wang et al., 2024).

The introduction of MARA systematically improves the MACE in force (F) prediction and in the majority of energy (E) prediction tasks (6 out of 10 molecules). Energy MAE reductions of up to 51% are observed, with an average reduction of about 11%, while force errors are consistently reduced by 3-10%, with an average improvement of about 6%.

These improvements allow MACE-MARA to achieve the lowest MAE for forces for 3 out of 10 molecules, compared to zero for the baseline model. For energy predictions, MARA allows MACE to achieve the first place for 3 out of 10 molecules, whereas the baseline only reaches a single second-place ranking. These results are obtained on a wide

Table 2. Tail-sensitive force errors (MAE in kcal/mol/Å) on the rMD17 benchmark, highlighting model robustness for molecular dynamics applications. We report Q₉₅, Q₉₉, and MAX for both MACE baseline and MACE-MARA across all molecules, including the relative differences (Δ) expressed as percentages.

MODEL	METRIC	ASPIRIN	AZOBENZ.	BENZENE	ETHANOL	MALONAL.	NAPHTHA.	PARACET.	SAL. ACID	TOULENE	URACIL
BASELINE	Q ₉₅	0.4739	0.2327	0.0240	0.1917	0.3454	0.1182	0.3556	0.2314	0.1157	0.1648
	Q ₉₉	0.5330	0.2661	0.0274	0.2347	0.3978	0.1368	0.4027	0.2657	0.1314	0.1890
	MAX	1.2985	0.6496	0.0988	1.2049	1.5461	0.2885	1.5136	1.1571	0.3710	0.7688
MARA	Q ₉₅	0.4393	0.2211	0.0224	0.1805	0.3290	0.1154	0.3341	0.2122	0.1087	0.1593
	Q ₉₉	0.5028	0.2526	0.0260	0.2108	0.3867	0.1312	0.3762	0.2397	0.1246	0.1859
	MAX	1.0071	0.5829	0.0808	0.8897	0.9987	0.3102	1.2903	1.0989	0.3497	0.6019
$\Delta(\%)$	Q ₉₅	-7.31	-4.99	-6.67	-5.84	-4.73	-2.37	-6.12	-8.30	-6.11	-3.31
	Q ₉₉	-5.67	-5.09	-5.11	-10.21	-2.79	-4.12	-6.57	-9.76	-5.17	-1.64
	MAX	-22.44	-10.27	-18.18	-26.16	-35.42	+7.52	-14.76	-5.05	-5.67	-21.73

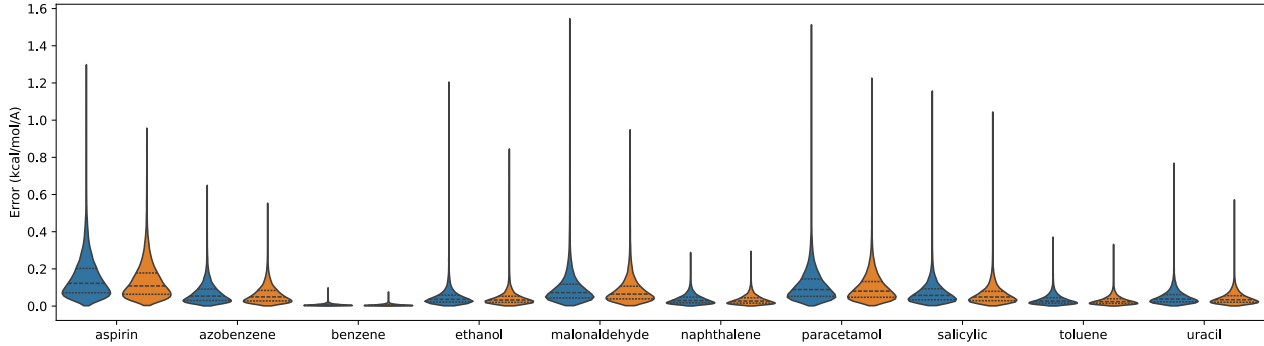


Figure 3. Violin plots of force error distributions for rMD17 molecules. Blue violins represent the MACE baseline, and orange represent MACE-MARA. Each molecule shows separate distributions for the two models, illustrating the overall error spread.

variety of chemical systems, ranging from small aromatic molecules to flexible structures with hydrogen bonds.

Although no model dominates both tasks, MACE enhanced with MARA ranks second on average in energy and force predictions, outperforming the MACE baseline and matching the performance of the latest state-of-the-art models.

4.2. Tail-risk and error distribution analysis

While the MAE is the standard metric for evaluating machine learning force fields, previous studies have shown that it does not fully capture model behavior in molecular dynamics settings (Fu et al., 2023; Duangdangchote et al., 2024). In these contexts, beyond average force accuracy, controlling the distribution of errors is crucial, since the accumulation of rare but large errors can drive the system toward unphysical configurations and compromise simulation stability (Wang et al., 2023b; Maheshwari et al., 2025).

To investigate this, we analyze error distributions both qualitatively and quantitatively, using tail-sensitive metrics: the 95th percentile error (Q₉₅), the 99th percentile error (Q₉₉), and the maximum observed error (MAX). Table 2 reports these metrics for MACE-MARA and the MACE baseline across all molecules in the rMD17 dataset.

The introduction of MARA consistently improves Q₉₅ and Q₉₉ across all systems, with average reductions of 5.58% and 5.51%, respectively, indicating a systematic mitigation of high-error events. Improvements are also observed for the maximum error in most molecules, with an average reduction of 15.12%. A single exception occurs for naphthalene, where the maximum error increases by 7.52%; however, this effect is confined to the extreme tail and does not affect Q₉₅ or Q₉₉, which remain improved.

Overall, these results suggest that MARA reduces both tail and worst-case errors, complementing the improvements in mean accuracy. This reduction in extreme errors lowers the risk that rare, high-magnitude deviations adversely impact molecular dynamics simulations, thereby enhancing model robustness in practical applications. To assess the practical impact of MARA, we conduct a molecular dynamics (MD) simulation test (details in Appendix E).

4.3. Ablations

We conduct ablation studies to analyze the impact of key hyperparameters of MACE-MARA on performance. All experiments are performed in a deterministic setting, keeping all conditions fixed except for the parameter under investigation. We consider two orthogonal experiments.

Table 3. Ablation study on the effect of the angular momentum order (ℓ) in MACE-MARA. Energy (E, in kcal/mol) and force (F, in kcal/mol/Å) mean absolute errors are reported for different ℓ values across selected molecules, comparing the baseline MACE and the MACE-MARA. Relative differences (Δ) indicate the impact of the module at each order.

MOLECULE	ATOMS	$\ell=1$			$\ell=2$			$\ell=3$		
		MACE	MACE-MARA	Δ (%)	MACE	MACE-MARA	Δ (%)	MACE	MACE-MARA	Δ (%)
ETHANOL	9	E 0.0061	0.0045	-26.23	0.0031	0.0037	+19.35	0.0032	0.0026	-18.75
		F 0.0517	0.0474	-8.32	0.0504	0.0458	-9.13	0.0484	0.0459	-5.17
PARACETAMOL	20	E 0.0916	0.0616	-32.75	0.0347	0.0284	-18.16	0.0300	0.0265	-11.67
		F 0.1164	0.1134	-2.58	0.1114	0.1072	-3.71	0.1107	0.1054	-4.77
AC-ALA3-NHMe	42	E 0.0782	0.0822	+5.13	0.0871	0.0821	-5.74	0.0883	0.0803	-9.02
		F 0.1322	0.1319	-0.23	0.1219	0.1197	-1.81	0.1230	0.1213	-1.30
STACHYOSE	87	E 0.1223	0.1223	0.00	0.1044	0.1154	+10.54	0.1325	0.1074	-18.93
		F 0.1791	0.1724	-3.74	0.1635	0.1534	-6.16	0.1634	0.1524	-6.77

Table 4. Ablation study on the effect of grid resolution for MACE-MARA ($\ell = 2$) on Paracetamol. Energy (E, kcal/mol) and force (F, kcal/mol/Å) MAEs are reported, along with inference time per batch (ms). Percentage differences ($\Delta\%$) are relative to the baseline Paracetamol $\ell = 2$ model.

	GRID SIZE				
	2 × 2	2 × 4	4 × 4	4 × 8	8 × 8
N. POINTS	4	8	16	32	64
ENERGY	0.0332	0.0411	0.0379	0.0284	0.0300
Δ ENERGY (%)	-4.33	+18.44	+9.22	-18.16	-13.54
FORCE	0.1089	0.1057	0.1075	0.1072	0.1045
Δ FORCE (%)	-2.24	-5.13	-3.43	-3.73	-6.21
TIME (ms)	111.67	112.74	114.15	117.97	128.18
Δ TIME (%)	+9.37	+10.42	+11.80	+15.54	+25.54

Effect of the harmonic order ℓ First, we vary the harmonic order ℓ , which determines the angular resolution of the model. Larger values of ℓ enable the representation of finer geometric details at the cost of increased computational complexity, while smaller values reduce angular resolution. Table 3 reports energy (E) and force (F) mean absolute errors for selected molecules, comparing the MACE baseline with MACE-MARA.

Across the rMD17 and MD22 datasets, MARA, using a 4×8 grid, consistently improves force predictions and generally enhances energy predictions. Larger and more flexible molecules tend to benefit more from higher angular resolution, whereas lower ℓ values are sufficient for smaller and more rigid molecules. These trends indicate that, by varying ℓ , the module continues to effectively capture angular dependencies across molecules of different sizes and complexities, providing a robust and scalable improvement over the baseline.

Effect of grid resolution Second, we fix $\ell = 2$ and vary the grid resolution for Paracetamol (Table 4). Percentage differences are shown relative to the baseline Paracetamol $\ell = 2$ model (Table 3). Increasing the number of grid points

improves both energy and force predictions, with the 4×8 and 8×8 grids achieving the largest gains. As expected, finer grids also increase computational cost: inference wall-clock time per batch rises by +9.4% for a 2×2 grid and +25% for 8×8 relative to the baseline, measured on an NVIDIA RTX 4090, with an average increase of 14.5%. These results highlight the trade-off between accuracy and efficiency and confirm that MARA enhances performance across grid configurations.

Taken together, these ablation experiments demonstrate that MARA provides robust improvements across both angular and radial resolutions, enhancing force and energy predictions consistently while balancing accuracy and computational costs depending on molecular size and complexity.

4.4. Interpretability of attention maps

In this section, we analyze the model through attention map analysis, using malonaldehyde as a case study. Two experiments are conducted to explore the effect of MARA’s attention on atomic movement.

In the first experiment, we study the intramolecular proton transfer in malonaldehyde, a process involving one hydrogen atom and two oxygen atoms (Schröder et al., 2011). This transfer occurs through a proton hopping mechanism that leverages hydrogen bonds and quantum tunneling phenomena, with a timescale on the order of femtoseconds (Zhou et al., 2025). We simulate the process by moving the hydrogen atom H_1 between the two oxygen atoms in 100 steps, recording the attention that the hydrogen atom receives from the surrounding oxygen (O_1, O_2) and carbon (C_1, C_2, C_3) atoms. The results, shown in Figure 4a, reveal that the radial slice of the attention map is symmetric around the saddle point, with carbon atoms exerting more attention on hydrogen compared to the oxygen atoms. Additionally, the intensity of attention varies as a function of the distance between the atoms.

In the second experiment, we examine attention in relation to angular geometry. The distance between C_3 and H_3

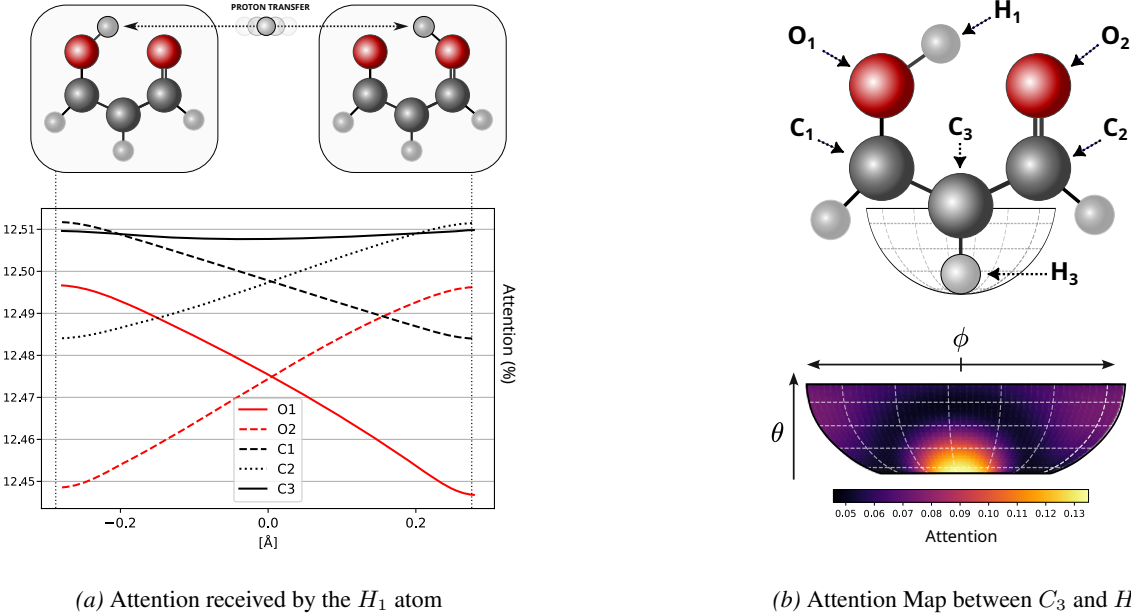


Figure 4. Interpretability of MARA. (a) Radial slice of the attention map showing attention from heavy atoms (O_1, O_2, C_1, C_2, C_3) to hydrogen (H_1) during intramolecular proton transfer. (b) Angular slice of the attention map showing attention between C_3 and H_3 as H_3 is rotated around C_3 at a fixed distance of 1 Å

is fixed at 1 Å, and the hydrogen atom is rotated around carbon C_3 , forming a hemisphere. Attention between the two atoms is monitored at each rotation angle. The angular slices of the attention map, shown in Figure 4b, reveal that attention intensity is maximized at a specific angle between the two atoms and varies significantly with the angle. This confirms that attention depends not only on distance but also on angular geometry, consistent with findings from the chemical literature (Linker et al., 2020; Fernández et al., 2023).

These results suggest that MARA, in addition to improving and stabilizing the performance of SE(3)-equivariant models, could be valuable in computational chemistry for analyzing complex angular and radial patterns in molecular interactions.

5. Conclusion

In this work, we introduce Modular Angular-Radial Attention (MARA), a continuous spherical attention mechanism that provides an efficient approximation to SE(3)-equivariant interactions in MLFF models. MARA operates directly on the angular and radial coordinates of atomic neighbors, enabling flexible and modular geometric weighting of local interactions.

Its plug-and-play integration, as demonstrated for MACE, requires no modifications to the underlying model, making

it suitable for other SE(3)-equivariant architectures. The method consistently improves accuracy and robustness in the prediction of forces, while also reducing high-error cases. These results suggest that MARA is an effective and generalizable operator capable of enhancing the expressiveness of atomistic models, with potential impact on the stability and reliability of atomistic simulations.

Limitations and future work. MARA provides an efficient approximation to SE(3)-equivariant interactions via spherical discretization and local neighborhood cutoffs. This introduces tunable parameters such as grid resolution, enabling a controllable trade-off between accuracy and computational cost depending on the complexity of the system. Our evaluation focuses on molecular benchmarks using a single host architecture as the primary backbone. While we demonstrate the portability of MARA by integrating it into other SE(3)-equivariant models (see Appendix F), broader validation on diverse chemical systems and different architectural paradigms remains future work.

Impact Statement

This paper presents work whose goal is to advance the field of Machine Learning. There are many potential societal consequences of our work, none of which we feel must be specifically highlighted here.

Acknowledgment

This study is funded by the Swiss National Science Foundation (SNSF) - Project Nr 200020 219388.

References

An, J., Lu, X., Qu, C., Shi, Y., Lin, P., Tang, Q., Xu, L., Cao, F., and Qi, Y. Equivariant spherical transformer for efficient molecular modeling. *CoRR*, abs/2505.23086, 2025. doi: 10.48550/ARXIV.2505.23086. URL <https://doi.org/10.48550/arXiv.2505.23086>.

Bahn, S. R. and Jacobsen, K. W. An object-oriented scripting interface to a legacy electronic structure code. *Comput. Sci. Eng.*, 4(3):56–66, MAY-JUN 2002. ISSN 1521-9615. doi: 10.1109/5992.998641.

Bartók, A. P., Payne, M. C., Kondor, R., and Csányi, G. Gaussian approximation potentials: The accuracy of quantum mechanics, without the electrons. *Physical review letters*, 104(13):136403, 2010.

Batatia, I., Batzner, S., Kovács, D. P., Musaelian, A., Simm, G. N. C., Drautz, R., Ortner, C., Kozinsky, B., and Csányi, G. The design space of $e(3)$ -equivariant atom-centered interatomic potentials, 2022a.

Batatia, I., Kovacs, D. P., Simm, G. N. C., Ortner, C., and Csanyi, G. MACE: Higher order equivariant message passing neural networks for fast and accurate force fields. In Oh, A. H., Agarwal, A., Belgrave, D., and Cho, K. (eds.), *Advances in Neural Information Processing Systems*, 2022b. URL <https://openreview.net/forum?id=YPpSngE-ZU>.

Batatia, I., Benner, P., Chiang, Y., Elena, A. M., Kovács, D. P., Riebesell, J., Advincula, X. R., Asta, M., Avaylon, M., Baldwin, W. J., Berger, F., Bernstein, N., Bhowmik, A., Bigi, F., Blau, S. M., Cărare, V., Ceriotti, M., Chong, S., Darby, J. P., De, S., Della Pia, F., Deringer, V. L., Elijošius, R., El-Machachi, Z., Fako, E., Falcioni, F., Ferrari, A. C., Gardner, J. L. A., Gawkowski, M. J., Genreith-Schriever, A., George, J., Goodall, R. E. A., Grandel, J., Grey, C. P., Grigorev, P., Han, S., Handley, W., Heenen, H. H., Hermansson, K., Ho, C. H., Hofmann, S., Holm, C., Jaafar, J., Jakob, K. S., Jung, H., Kapil, V., Kaplan, A. D., Karimitari, N., Kermode, J. R., Kourtis, P., Kroupa, N., Kullgren, J., Kuner, M. C., Kuryla, D., Liepuoniute, G., Lin, C., Margraf, J. T., Magdău, I.-B., Michaelides, A., Moore, J. H., Naik, A. A., Niblett, S. P., Norwood, S. W., O'Neill, N., Ortner, C., Persson, K. A., Reuter, K., Rosen, A. S., Rosset, L. A. M., Schaaf, L. L., Schran, C., Shi, B. X., Sivonxay, E., Stenczel, T. K., Sutton, C., Svahn, V., Swinburne, T. D., Tilly, J., van der Oord, C., Vargas, S., Varga-Umbrich, E., Vegge, T., Vondrák, M., Wang, Y., Witt, W. C., Wolf, T., Zills, F., and Csányi, G. A foundation model for atomistic materials chemistry. *Journal of Chemical Physics*, 163(18), 11 2025. doi: 10.1063/5.0297006.

Batzner, S. L., Smidt, T. E., Sun, L., Mailoa, J. P., Kornbluth, M., Molinari, N., and Kozinsky, B. $Se(3)$ -equivariant graph neural networks for data-efficient and accurate interatomic potentials. *CoRR*, abs/2101.03164, 2021. URL <https://arxiv.org/abs/2101.03164>.

Behler, J. Perspective: Machine learning potentials for atomistic simulations. *The Journal of Chemical Physics*, 145(17):170901, 11 2016. ISSN 0021-9606. doi: 10.1063/1.4966192. URL <https://doi.org/10.1063/1.4966192>.

Behler, J. and Parrinello, M. Generalized neural-network representation of high-dimensional potential-energy surfaces. *Physical review letters*, 98(14):146401, 2007.

Benny, Y. and Wolf, L. Sphereuformer: A u-shaped transformer for spherical 360 perception. In *IEEE/CVF Conference on Computer Vision and Pattern Recognition, CVPR 2025, Nashville, TN, USA, June 11-15, 2025*, pp. 940–950, 2025. doi: 10.1109/CVPR52734.2025.00096. URL https://openaccess.thecvf.com/content/CVPR2025/html/Benny_SphereUFormer_A_U-Shaped_Transformer_for_Spherical_360_Perception_CVPR_2025_paper.html.

Bonev, B., Kurth, T., Hundt, C., Pathak, J., Baust, M., Kashinath, K., and Anandkumar, A. Spherical fourier neural operators: Learning stable dynamics on the sphere, 2023.

Bonev, B., Rietmann, M., Paris, A., Carpentieri, A., and Kurth, T. Attention on the sphere. *CoRR*, abs/2505.11157, 2025. doi: 10.48550/ARXIV.2505.11157. URL <https://doi.org/10.48550/arXiv.2505.11157>.

Botu, V., Batra, R., Chapman, J., and Ramprasad, R. Machine learning force fields: Construction, validation, and outlook. *The Journal of Physical Chemistry C*, 121(1):511–522, 2017. doi: 10.1021/acs.jpcc.6b10908. URL <https://doi.org/10.1021/acs.jpcc.6b10908>.

Brody, S., Alon, U., and Yahav, E. How attentive are graph attention networks? In *The Tenth International Conference on Learning Representations, ICLR 2022, Virtual Event, April 25-29, 2022*. OpenReview.net, 2022. URL <https://openreview.net/forum?id=F72ximsx7C1>.

Bronstein, M. M., Bruna, J., Cohen, T., and Velickovic, P. Geometric deep learning: Grids, groups, graphs, geodesics, and gauges. *CoRR*, abs/2104.13478, 2021. URL <https://arxiv.org/abs/2104.13478>.

Cheng, Z., Zhao, D., Ma, J., Li, W., and Li, S. An on-the-fly approach to construct generalized energy-based fragmentation machine learning force fields of complex systems. *The Journal of Physical Chemistry A*, 124(24):5007–5014, 2020. doi: 10.1021/acs.jpca.0c04526. URL <https://doi.org/10.1021/acs.jpca.0c04526>. PMID: 32459485.

Chmiela, S., Tkatchenko, A., Sauceda, H. E., Poltavsky, I., Schütt, K. T., and Müller, K.-R. Machine learning of accurate energy-conserving molecular force fields. *Science advances*, 3(5):e1603015, 2017.

Chmiela, S., Sauceda, H. E., Müller, K.-R., and Tkatchenko, A. Towards exact molecular dynamics simulations with machine-learned force fields. *Nature communications*, 9(1):3887, 2018.

Chmiela, S., Vassilev-Galindo, V., Unke, O. T., Kabylda, A., Sauceda, H. E., Tkatchenko, A., and Müller, K.-R. Accurate global machine learning force fields for molecules with hundreds of atoms. *Science Advances*, 9(2):eadf0873, 2023.

Cho, S., Jung, R., and Kwon, J. Spherical transformer. *CoRR*, abs/2202.04942, 2022. URL <https://arxiv.org/abs/2202.04942>.

Christensen, A. S. and von Lilienfeld, O. A. On the role of gradients for machine learning of molecular energies and forces. *Mach. Learn. Sci. Technol.*, 1(4):45018, 2020. doi: 10.1088/2632-2153/ABBA6F. URL <https://doi.org/10.1088/2632-2153/abba6f>.

Duangdangchote, S., Seferos, D. S., and Voznyy, O. Stability and transferability of machine learning force fields for molecular dynamics applications††electronic supplementary information (esi) available. see doi: <https://doi.org/10.1039/d4dd00140k>. *Digital Discovery*, 3(11):2177–2182, 2024. ISSN 2635-098X. doi: <https://doi.org/10.1039/d4dd00140k>. URL <https://www.sciencedirect.com/science/article/pii/S2635098X24001736>.

Duval, A., Mathis, S. V., Joshi, C. K., Schmidt, V., Miret, S., Malliaros, F. D., Cohen, T., Lio, P., Bengio, Y., and Bronstein, M. A hitchhiker’s guide to geometric gnns for 3d atomic systems. *arXiv preprint arXiv:2312.07511*, 2023.

Fernández, I., Bickelhaupt, F. M., and Svatunek, D. Unraveling the bürgi-dunitz angle with precision: The power of a two-dimensional energy decomposition analysis. *Journal of Chemical Theory and Computation*, 19(20):7300–7306, 2023. doi: 10.1021/acs.jctc.3c00907. URL <https://doi.org/10.1021/acs.jctc.3c00907>. PMID: 37791978.

Frank, J. T., Unke, O. T., Müller, K.-R., and Chmiela, S. A euclidean transformer for fast and stable machine learned force fields. *Nature Communications*, 15(1):6539, 2024.

Fu, X., Wu, Z., Wang, W., Xie, T., Keten, S., Gómez-Bombarelli, R., and Jaakkola, T. S. Forces are not enough: Benchmark and critical evaluation for machine learning force fields with molecular simulations. *Trans. Mach. Learn. Res.*, 2023, 2023. URL <https://openreview.net/forum?id=A8pqQipwkt>.

Fuchs, F., Worrall, D. E., Fischer, V., and Welling, M. Se(3)-transformers: 3d roto-translation equivariant attention networks. In Larochelle, H., Ranzato, M., Hadsell, R., Balcan, M., and Lin, H. (eds.), *Advances in Neural Information Processing Systems 33: Annual Conference on Neural Information Processing Systems 2020, NeurIPS 2020, December 6-12, 2020, virtual*, 2020. URL <https://proceedings.neurips.cc/paper/2020/hash/15231a7ce4ba789d13b722cc5c955834-Abstract.html>.

Klicpera, J., Groß, J., and Günnemann, S. Directional message passing for molecular graphs. In *8th International Conference on Learning Representations, ICLR 2020, Addis Ababa, Ethiopia, April 26-30, 2020*. OpenReview.net, 2020. URL <https://openreview.net/forum?id=B1eWbxStPH>.

Langley, P. Crafting papers on machine learning. In Langley, P. (ed.), *Proceedings of the 17th International Conference on Machine Learning (ICML 2000)*, pp. 1207–1216, Stanford, CA, 2000. Morgan Kaufmann.

Larsen, A. H., Mortensen, J. J., Blomqvist, J., Castelli, I. E., Christensen, R., Dułak, M., Friis, J., Groves, M. N., Hammer, B., Hargas, C., Hermes, E. D., Jennings, P. C., Jensen, P. B., Kermode, J., Kitchin, J. R., Kolsbjerg, E. L., Kubal, J., Kaasbjerg, K., Lysgaard, S., Maransson, J. B., Maxson, T., Olsen, T., Pastewka, L., Petersen, A., Rostgaard, C., Schiøtz, J., Schütt, O., Strange, M., Thygesen, K. S., Vegge, T., Vilhelmsen, L., Walter, M., Zeng, Z., and Jacobsen, K. W. The atomic simulation environment—a python library for working with atoms. *Journal of Physics: Condensed Matter*, 29(27):273002, 2017. URL <http://stacks.iop.org/0953-8984/29/i=27/a=273002>.

Liao, Y. and Smidt, T. E. Equiformer: Equivariant graph attention transformer for 3d atomistic graphs. In *The*

Eleventh International Conference on Learning Representations, ICLR 2023, Kigali, Rwanda, May 1-5, 2023. OpenReview.net, 2023. URL <https://openreview.net/forum?id=KwmPfARgOTD>.

Liao, Y., Wood, B. M., Das, A., and Smidt, T. E. Equiformer2: Improved equivariant transformer for scaling to higher-degree representations. In *The Twelfth International Conference on Learning Representations, ICLR 2024, Vienna, Austria, May 7-11, 2024*. OpenReview.net, 2024. URL <https://openreview.net/forum?id=mCOBKZmrzD>.

Linker, G.-J., van Duijnen, P. T., and Broer, R. Understanding trends in molecular bond angles. *The Journal of Physical Chemistry A*, 124(7):1306–1311, 2020. doi: 10.1021/acs.jpca.9b10248. URL <https://doi.org/10.1021/acs.jpca.9b10248>. PMID: 31986041.

Maheshwari, S., Ock, J., Kolluru, A., Farimani, A. B., and Kitchin, J. R. Beyond force metrics: Pre-training mlfss for stable MD simulations. *CoRR*, abs/2506.14850, 2025. doi: 10.48550/ARXIV.2506.14850. URL <https://doi.org/10.48550/arXiv.2506.14850>.

Musaelian, A., Batzner, S. L., Johansson, A., Sun, L., Owen, C. J., Kornbluth, M., and Kozinsky, B. Learning local equivariant representations for large-scale atomistic dynamics. *CoRR*, abs/2204.05249, 2022. doi: 10.48550/ARXIV.2204.05249. URL <https://doi.org/10.48550/arXiv.2204.05249>.

Qiao, Z., Christensen, A. S., Welborn, M., Manby, F. R., Anandkumar, A., and Miller, T. F. Informing geometric deep learning with electronic interactions to accelerate quantum chemistry. *Proceedings of the National Academy of Sciences*, 119(31):e2205221119, 2022. doi: 10.1073/pnas.2205221119. URL <https://www.pnas.org/doi/abs/10.1073/pnas.2205221119>.

Satorras, V. G., Hoogeboom, E., and Welling, M. E(n) equivariant graph neural networks. In Meila, M. and Zhang, T. (eds.), *Proceedings of the 38th International Conference on Machine Learning, ICML 2021, 18-24 July 2021, Virtual Event*, volume 139 of *Proceedings of Machine Learning Research*, pp. 9323–9332. PMLR, 2021. URL <http://proceedings.mlr.press/v139/satorras21a.html>.

Schröder, M., Gatti, F., and Meyer, H.-D. Theoretical studies of the tunneling splitting of malonaldehyde using the multiconfiguration time-dependent hartree approach. *The Journal of chemical physics*, 134:234307, 06 2011. doi: 10.1063/1.3600343.

Schütt, K., Kindermans, P., Felix, H. E. S., Chmiela, S., Tkatchenko, A., and Müller, K. Schnet: A continuous-filter convolutional neural network for modeling quantum interactions. In Guyon, I., von Luxburg, U., Bengio, S., Wallach, H. M., Fergus, R., Vishwanathan, S. V. N., and Garnett, R. (eds.), *Advances in Neural Information Processing Systems 30: Annual Conference on Neural Information Processing Systems 2017, December 4-9, 2017, Long Beach, CA, USA*, pp. 991–1001, 2017. URL <https://proceedings.neurips.cc/paper/2017/hash/303ed4c69846ab36c2904d3ba8573050-Abstract.html>.

Shapeev, A. V. Moment tensor potentials: A class of systematically improvable interatomic potentials. *Multiscale Modeling & Simulation*, 14(3):1153–1173, 2016. doi: 10.1137/15M1054183. URL <https://doi.org/10.1137/15M1054183>.

Thomas, N., Smidt, T. E., Kearnes, S., Yang, L., Li, L., Kohlhoff, K., and Riley, P. Tensor field networks: Rotation- and translation-equivariant neural networks for 3d point clouds. *CoRR*, abs/1802.08219, 2018. URL <http://arxiv.org/abs/1802.08219>.

Thompson, A., Swiler, L., Trott, C., Foiles, S., and Tucker, G. Spectral neighbor analysis method for automated generation of quantum-accurate interatomic potentials. *Journal of Computational Physics*, 285:316–330, 2015. ISSN 0021-9991. doi: <https://doi.org/10.1016/j.jcp.2014.12.018>. URL <https://www.sciencedirect.com/science/article/pii/S0021999114008353>.

Unke, O. T., Chmiela, S., Sauceda, H. E., Gastegger, M., Poltavsky, I., Schütt, K. T., Tkatchenko, A., and Müller, K.-R. Machine learning force fields. *Chemical Reviews*, 121(16):10142–10186, 2021. doi: 10.1021/acs.chemrev.0c01111. URL <https://doi.org/10.1021/acs.chemrev.0c01111>. PMID: 33705118.

Vaswani, A., Shazeer, N., Parmar, N., Uszkoreit, J., Jones, L., Gomez, A. N., Kaiser, L., and Polosukhin, I. Attention is all you need. In *Advances in Neural Information Processing Systems 30: Annual Conference on Neural Information Processing Systems 2017, December 4-9, 2017, Long Beach, CA, USA*, pp. 5998–6008, 2017. URL <https://proceedings.neurips.cc/paper/2017/hash/3f5ee243547dee91fb053c1c4a845aa-Abstract.html>.

Velickovic, P., Cucurull, G., Casanova, A., Romero, A., Liò, P., and Bengio, Y. Graph attention networks. In *6th International Conference on Learning Representations, ICLR 2018, Vancouver, BC, Canada, April 30 - May 3*,

2018, *Conference Track Proceedings*. OpenReview.net,
2018. URL <https://openreview.net/forum?id=rJXMpikCZ>.

Wang, Y., Wang, T., Li, S., He, X., Li, M., Wang, Z.,
Zheng, N., Shao, B., and Liu, T. Enhancing geometric
representations for molecules with equivariant vector-
scalar interactive message passing. *Nature Communications*, 15(1):313, 2024. doi: 10.1038/s41467-023-43720-
2. URL <https://www.nature.com/articles/s41467-023-43720-2>.

Wang, Z., Liu, G., Zhou, Y., Wang, T., and Shao, B.
Efficiently incorporating quintuple interactions into
geometric deep learning force fields. In Oh, A.,
Naumann, T., Globerson, A., Saenko, K., Hardt,
M., and Levine, S. (eds.), *Advances in Neural Infor-
mation Processing Systems 36: Annual Conference
on Neural Information Processing Systems 2023,
NeurIPS 2023, New Orleans, LA, USA, December
10 - 16, 2023*, 2023a. URL http://papers.nips.cc/paper_files/paper/2023/hash/f32b13bfc384b3b1d52d675b05f2bece-Abstract-Conference.html.

Wang, Z., Wu, H., Sun, L., He, X., Liu, Z., Shao, B., Wang,
T., and Liu, T.-Y. Improving machine learning force fields
for molecular dynamics simulations with fine-grained
force metrics. *The Journal of Chemical Physics*, 159
(3):035101, 07 2023b. ISSN 0021-9606. doi: 10.1063/
5.0147023. URL <https://doi.org/10.1063/5.0147023>.

Zhou, J., Wu, L., Belina, M., Skitnevskaya, A. D., Jia, S.,
Xue, X., Hao, X., Zeng, Q., Ma, Q., Zhao, Y., et al. State-
and time-resolved observation of ultrafast intermolecular
proton transfer in hydrated biomolecules. *Nature Com-
munications*, 16(1):5838, 2025.

A. Mathematical Background

In this section, we provide the mathematical background for the constructions used in the main text. First, we discuss the basic properties of the two-dimensional sphere S^2 and the special orthogonal group $SO(3)$, which governs rotations in three-dimensional space. We then describe the special Euclidean group $SE(3)$, which represents the motions of rigid bodies, and finally introduce the grid field used in our algorithm along with its key properties, including scale linearity and invariance under rigid transformations.

A.1. Rotations on the 2-Sphere

We discuss some fundamental notions concerning the two-dimensional sphere S^2 and the rotation group $SO(3)$.

To define functions on the sphere, we require coordinates. A standard choice is to parametrize points $\mathbf{p} \in S^2$ using the colatitude $\theta \in [0, \pi]$ and the longitude $\varphi \in [0, 2\pi]$. In these coordinates, a unit vector \mathbf{p} can be expressed as

$$\mathbf{p} = (\cos(\varphi) \sin(\theta), \sin(\varphi) \sin(\theta), \cos(\theta))^T. \quad (9)$$

To discuss symmetries of the sphere, we consider the special orthogonal group $SO(3)$, which consists of all proper rotations in \mathbb{R}^3 . Elements of $SO(3)$ are 3×3 matrices with determinant one, whose inverses coincide with their transposes. Any rotation $R \in SO(3)$ can be written in terms of the Eulerian angles $\varphi \in [0, 2\pi], \theta \in [0, \pi], \psi \in [0, 2\pi]$, such that

$$R = R_z(\varphi)R_y(\theta)R_z(\psi), \quad (10)$$

where R_z and R_y are rotations around the z- and y-axes:

$$R_z(\varphi) = \begin{bmatrix} \cos \varphi & -\sin \varphi & 0 \\ \sin \varphi & \cos \varphi & 0 \\ 0 & 0 & 1 \end{bmatrix}, \quad R_y(\varphi) = \begin{bmatrix} \cos \varphi & 0 & \sin \varphi \\ 0 & 1 & 0 \\ -\sin \varphi & 0 & \cos \varphi \end{bmatrix}. \quad (11)$$

Unlike translations in the plane, rotations generally do not commute, making $SO(3)$ non-abelian. Rotations in $SO(3)$ can reach any point on the sphere. In particular, applying a rotation to the north pole $n = (0, 0, 1)^T$ yields

$$Rn = R_z(\varphi)R_y(\theta)R_z(\psi)n = (\cos(\varphi) \sin(\theta), \sin(\varphi) \sin(\theta), \cos(\theta))^T. \quad (12)$$

We observe that the last rotation angle ψ is dropped, illustrating that S^2 can be obtained as the quotient of $SO(3)$ and $SO(2)$.

A.2. Rigid motions and the special euclidean group

The special euclidean group $SE(3)$ describes all rigid body motions in three-dimensional space, combining rotations and translations. Each element of $SE(3)$ can be represented as a pair (R, \mathbf{t}) , with $R \in SO(3)$ and $\mathbf{t} \in \mathbb{R}^3$, or equivalently as a 4×4 homogeneous transformation matrix:

$$T = \begin{bmatrix} R & \mathbf{t} \\ \mathbf{0}^T & 1 \end{bmatrix}. \quad (13)$$

Composition of two rigid motions corresponds to matrix multiplication:

$$T_1 T_2 = \begin{bmatrix} R_1 R_2 & R_1 \mathbf{t}_2 + \mathbf{t}_1 \\ \mathbf{0}^T & 1 \end{bmatrix}. \quad (14)$$

Unlike $SO(3)$, $SE(3)$ also includes translations. It is a six-dimensional, non-abelian Lie group: three degrees of freedom correspond to rotation, and three to translation. The subgroup of pure translations,

$$\mathbb{R}^3 \cong \{(\mathbb{I}_3, \mathbf{t}) \mid \mathbf{t} \in \mathbb{R}^3\}, \quad (15)$$

is normal in $SE(3)$, and the group can be expressed as a semi-direct product:

$$SE(3) \cong \mathbb{R}^3 \rtimes SO(3). \quad (16)$$

Rigid motions in $SE(3)$ are fundamental in robotics, computer vision, and physics, as they describe the complete spatial displacement of a body in \mathbb{R}^3 . As a smooth Lie group, $SE(3)$ generalizes the rotational symmetries of $SO(3)$ to full rigid body transformations.

A.3. Properties of the grid field

Consider two points $\mathbf{p}_S, \mathbf{p}_T \in \mathbb{R}^3$ and define the vector connecting them:

$$\mathbf{v} = \mathbf{p}_S - \mathbf{p}_T, \quad d = \|\mathbf{v}\|, \quad \hat{\mathbf{u}} = \frac{\mathbf{v}}{d} \in S^2. \quad (17)$$

Let

$$\{g_k \in \mathbb{R}^3 : \|g_k\| = 1, k = 1, \dots, N\} \quad (18)$$

denote a set of points on the unit sphere S^2 . We define a scaled sphere of radius d centered at \mathbf{p}_S :

$$\mathbf{x}_k = \mathbf{p}_S + d g_k. \quad (19)$$

The distance from \mathbf{x}_k to \mathbf{p}_T is

$$\delta_k = \|\mathbf{x}_k - \mathbf{p}_T\| = \|(\mathbf{p}_S - \mathbf{p}_T) + d g_k\| = \|\mathbf{v} + d g_k\|. \quad (20)$$

Dividing by d and using the unit vector $\hat{\mathbf{u}} = \frac{\mathbf{v}}{d}$ gives a normalized distance:

$$\frac{\delta_k}{d} = \|\hat{\mathbf{u}} + g_k\|. \quad (21)$$

Expanding the norm yields

$$\delta_k = d \|\hat{\mathbf{u}} + g_k\| = d \sqrt{(\hat{\mathbf{u}} + g_k) \cdot (\hat{\mathbf{u}} + g_k)} = d \sqrt{2 + 2(\hat{\mathbf{u}} \cdot g_k)}. \quad (22)$$

Let θ_k denote the angle between $\hat{\mathbf{u}}$ and g_k , so that $\hat{\mathbf{u}} \cdot g_k = \cos \theta_k$. Then

$$\delta_k = d \sqrt{2(1 + \cos \theta_k)}. \quad (23)$$

In particular, the extreme cases are

$$\begin{cases} \cos \theta_k = 1 & \implies \delta_k = 2d \\ \cos \theta_k = -1 & \implies \delta_k = 0 \end{cases} \quad (24)$$

This shows that δ_k is linearly proportional to d for any θ_k . Under a rigid transformation

$$\mathbf{p}'_S = R\mathbf{p}_S + t, \quad \mathbf{p}'_T = R\mathbf{p}_T + t, \quad R \in SO(3), t \in \mathbb{R}^3, \quad (25)$$

the connecting vector transforms as

$$\mathbf{v}' = \mathbf{p}'_S - \mathbf{p}'_T = R\mathbf{v}. \quad (26)$$

Simultaneously, the unit sphere points are rotated: $g'_k = Rg_k$. Therefore, the distances δ_k are invariant under rigid transformations:

$$\delta'_k = \|\mathbf{v}' + d g'_k\| = \|R(\mathbf{v} + d g_k)\| = \|\mathbf{v} + d g_k\| = \delta_k. \quad (27)$$

Thus, the field defined by δ_k is linearly sensitive to the scale d and invariant under rigid body transformations.

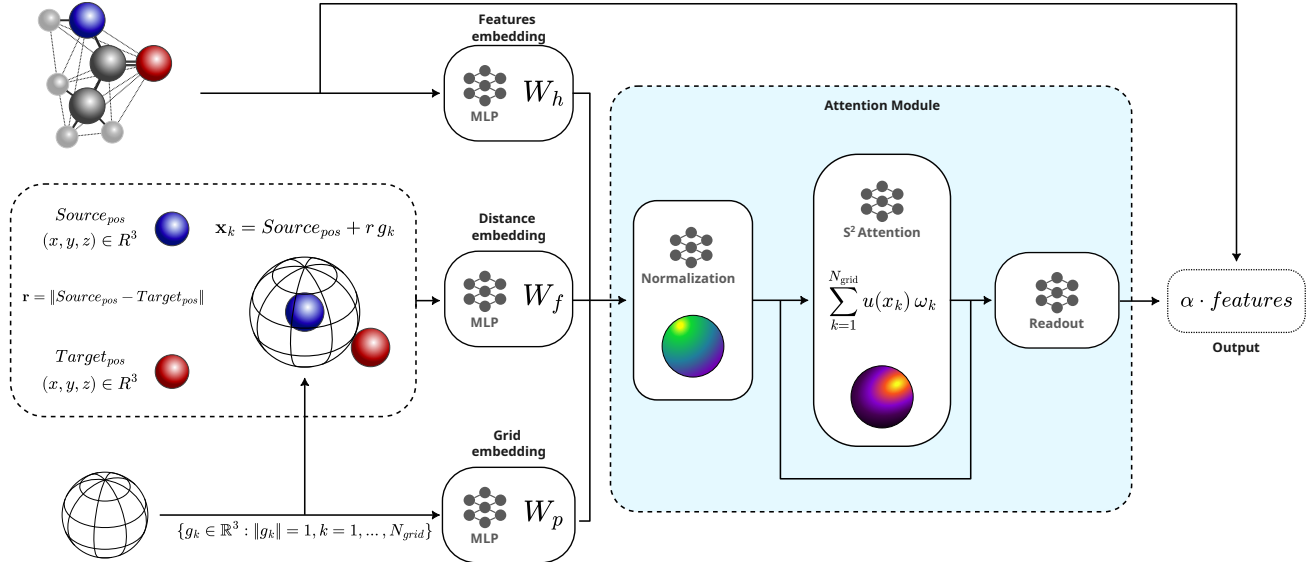


Figure 5. Module operating diagram

B. Architecture

For the implementation of our module, Python 3.10 with support for CUDA 12.8 and Torch 2.8.0 is used. For the spherical attention, the original implementation of Bonev et al. (2025) in the torch-harmonics 0.8.0 package, available online, is used (Bonev et al., 2023). The version of ACE/MACE suite (Batatia et al., 2022b;a) we use is the one in which the module is introduced in its original version. In addition, the cuEquivariance library has been used, which allows optimisations for CUDA on Torch.

The module is used with a 4×8 grid, with the exception of Table 4, for which we have modified the resolution to verify its impact. In MACE, the module is introduced in the RealAgnosticInteractionBlock and RealAgnosticResidualInteractionBlock blocks, as shown in Algorithm 1. The module returns the message already enriched by attention and separately the applied weights. Our module is publicly available at <https://github.com/monsieursolver/MARA> for further details and implementations. The model's functioning diagram is shown in the Figure 5.

Algorithm 1 Insertion of the module into the MACE blocks

```

1:  $m_{ji} \leftarrow \text{self.conv}_{tp}(\text{nodefeats}[\text{edgeindex}[0]], \text{edgeattrs}, \text{tpweights})$ 
2:  $m_{ji}, \text{att} \leftarrow \text{self.spherical_attention}(m_{ji}, \text{positions}, \text{edgeindex}, \text{edgefeats})$ 
3:  $\text{message} \leftarrow \text{scatter\_sum}(\text{src} = m_{ji}, \text{index} = \text{edgeindex}[1], \text{dim} = 0, \text{dim\_size} = \text{nodefeats.shape}[0])$ 

```

The model has been trained primarily on an NVIDIA H100, maintaining the same parameters used in the original paper, which uses an NVIDIA A100. Inference tests, on the other hand, have been performed using an RTX 4090.

C. Learnable positional encoding

We conduct a set of new ablation experiments to assess the contribution of learnable projections and positional encoding to the prediction of energies (E) and forces (F). We select four molecules with substantially different system sizes, fix $\ell = 2$, and use a 4×8 grid. For each molecule, we retrain the MACE-MARA under four configurations: (i) the full model, (ii) without positional encoding, (iii) with fixed (non-learnable) projections, and (iv) without positional encoding and with fixed projections.

Table 5. Ablation study on the effect of positional encoding and learnable projections for energy (E, MAE kcal/mol) and force (F, MAE kcal/mol/Å) prediction. We compare the MACE-MARA with variants that remove positional encoding, disable learning of the projections, or apply both modifications. Lower values indicate better performance.

LEARNABLE	NOT LEARNABLE	POSITIONAL ENCODING	ETHANOL	PARACETAMOL	AC-ALA3-NHME	STACHYOSE
✓	✓	E	0.0037	0.0284	0.0821	0.1154
		F	0.0458	0.1072	0.1197	0.1534
✓	✓	E	0.0036	0.0292	0.0745	0.1242
		F	0.0487	0.1084	0.1161	0.1564
✓		E	0.0028	0.0292	0.0728	0.1594
		F	0.0486	0.1081	0.1152	0.1557
✓		E	0.0036	0.0307	0.0711	0.1132
		F	0.0484	0.1125	0.1157	0.1555

The results, shown in Table 5, show that positional encoding and learnable projections generally improve force prediction performance, achieving lower mean absolute error on three of the four molecules considered. In contrast, for energy prediction, only one molecule achieves its minimum error in the same configuration. The best overall energy performance (two out of four molecules) is achieved with the opposite setting, i.e., without positional encoding and without learnable projections.

Finally, these results indicate that retaining positional encoding while disabling learning of the projections is not beneficial: this configuration does not achieve the best performance in any of the eight evaluated metrics.

D. Convergence study

Table 6. Test-set performance on MD22 DHA and AT-AT DNA base pairs for different training regimes. We compare MACE baseline and MACE-MARA with 100 and 10,000 samples, reporting errors on energies (E, MAE in kcal/mol) and forces (F, MAE in kcal/mol/Å).

MOLECULES	TRAINING SAMPLES = 100			TRAINING SAMPLES = 10K			
	BASELINE	MARA	Δ (%)	BASELINE	MARA	Δ (%)	
DHA	E	0.2685	0.2674	-0.41	0.1212	0.1204	-0.66
	F	0.4924	0.4796	-2.60	0.1245	0.1184	-4.90
AT-AT	E	0.1324	0.1511	+14.12	0.1482	0.1480	-0.13
	F	0.1759	0.1783	+1.36	0.1274	0.1209	-5.10

We further analyze two additional molecules from the MD22 dataset, specifically Docosahexaenoic Acid (DHA), consisting of 56 atoms, and AT-AT DNA base pairs, consisting of 60 atoms, in order to evaluate the performance of our model under conditions of data scarcity and abundance. The dataset comprises 69,744 and 19,999 molecular dynamics (MD) trajectories, respectively. From each set, we randomly sample 100 and 10,000 configurations for the training set, keeping 1,000 examples for validation and using all remaining configurations as the test set.

As shown in Table 6, performance – particularly in terms of force prediction – differs significantly between training with 100 examples and training with 10,000 examples. This behavior is expected: with a limited number of samples, the model has limited ability to learn less frequent configurations, leading to less accurate predictions. Furthermore, both molecules considered are highly flexible and have a large conformational space, making the problem particularly challenging in a low-data regime.

The results show that, with few training examples, the proposed module does not provide significant benefits and, in one case, even worsens the prediction of forces compared to the baseline model. On the other hand, when the number of samples is sufficiently high, the attention mechanism is particularly effective, improving performance in both tasks: on average, there is an improvement of about 5% in forces and about 0.4% in energies, the latter being considered a marginal gain. This pattern is further supported by Table 7, which analyzes the distributions of Q95, Q99, and MAX.

Table 7. Test-set performance on MD22 DHA and AT-AT DNA base pairs for different training regimes. We compare MACE baseline and MACE-MARA with 100 and 10,000 samples, reporting errors Q₉₅, Q₉₉ and max on forces (F, MAE in kcal/mol/Å).

MOLECULES	TRAINING SAMPLES = 100			TRAINING SAMPLES = 10K			
	BASELINE	MARA	Δ (%)	BASELINE	MARA	Δ (%)	
DHA	Q ₉₅	1.5110	1.4893	-1.44	0.3699	0.3511	-5.11
	Q ₉₉	2.5615	2.5436	-0.70	0.5936	0.5655	-4.73
	MAX	42.857	44.344	+3.47	5.2803	5.8291	+10.41
AT-AT	Q ₉₅	0.5385	0.5504	+2.21	0.3617	0.3423	-5.37
	Q ₉₉	0.9075	0.9250	+1.93	0.5483	0.5177	-5.59
	MAX	18.937	18.678	-1.36	6.1684	5.7134	-7.39

D.1. Convergence speed

To verify that attention provides a real benefit to the training process, we analyze the model’s performance at each epoch on the validation set of 1000 examples, displaying both the loss and the corresponding RMSE on both forces and energies. In both configurations, the models are trained for 100k gradient steps, allowing them to reach a condition of near convergence.

To quantify the benefit of introducing MARA, we also display the relative ratio between the MACE-Baseline model and MACE-MARA, defined as:

$$\frac{\text{MACE-Baseline} - \text{MACE-MARA}}{\text{MACE-Baseline}} \cdot 100.$$

In this case, positive values indicate that MACE-MARA performs better than MACE-Baseline, while negative values indicate that MACE-Baseline is superior, as it has an error closer to zero.

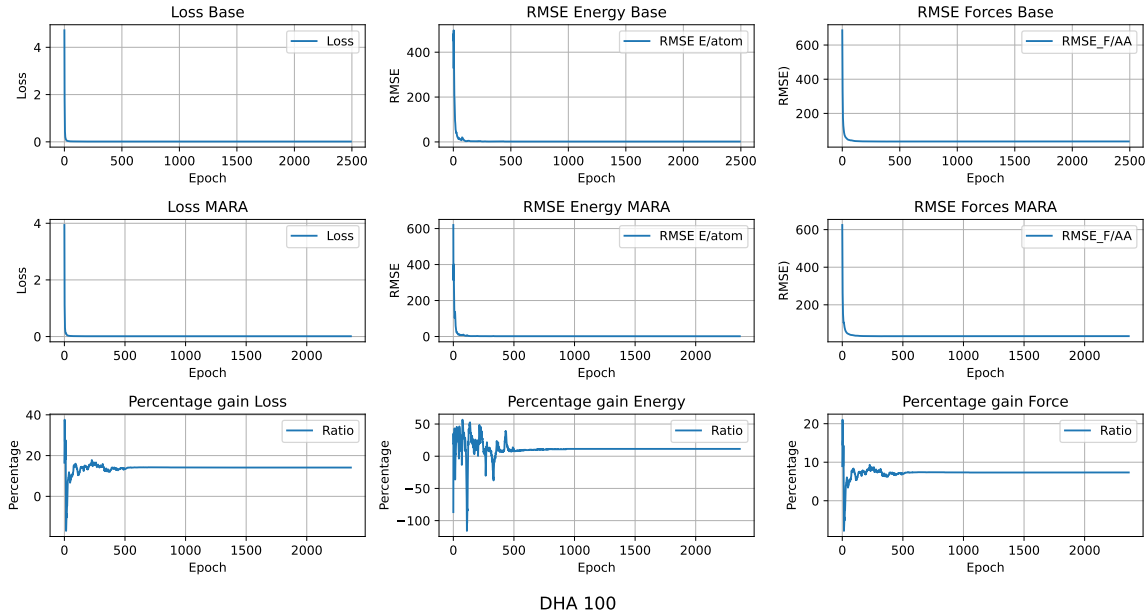


Figure 6. Performance of models on the validation set on DHA with 100 samples. The subplots show, from left to right, Loss, Energy, and Strength; from top to bottom, Baseline, MARA, and the percentage ratio.

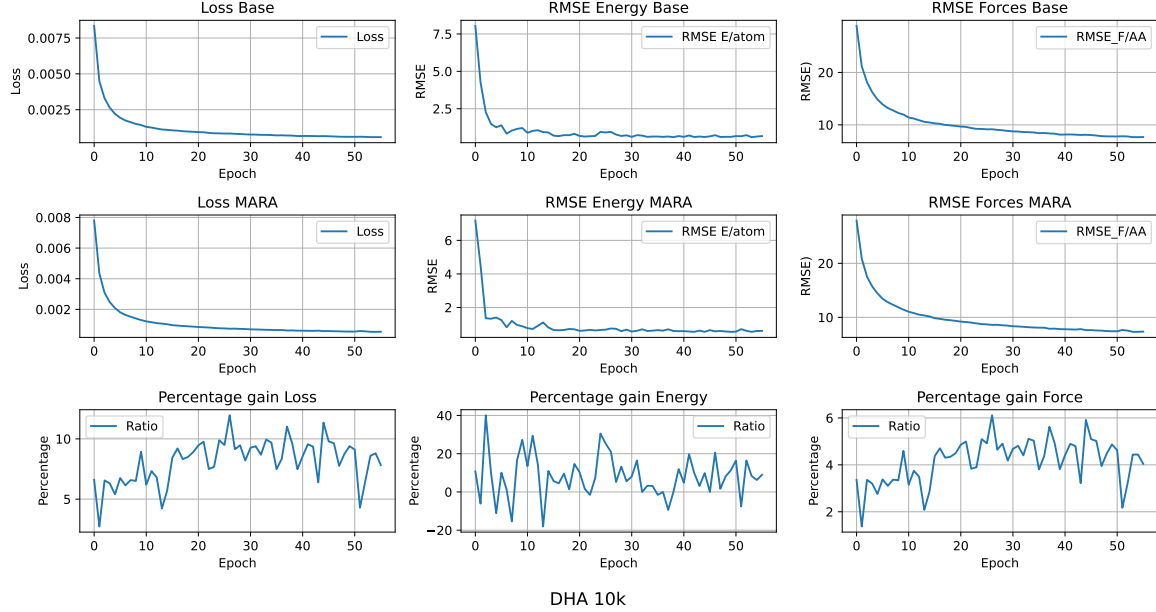


Figure 7. Performance of models on the validation set on DHA with 10,000 samples. The subplots show, from left to right, Loss, Energy, and Strength; from top to bottom, Baseline, MARA, and the percentage ratio.

Figures 6 and 7 show that, for Docosahexaenoic Acid (DHA), the validation ratio is positive in both configurations, leading to an advantage in the testing phase. Notably, as training examples increase, MARA maintains a positive ratio, especially in force prediction, benefiting from early epochs and progressively amplifying the advantage.

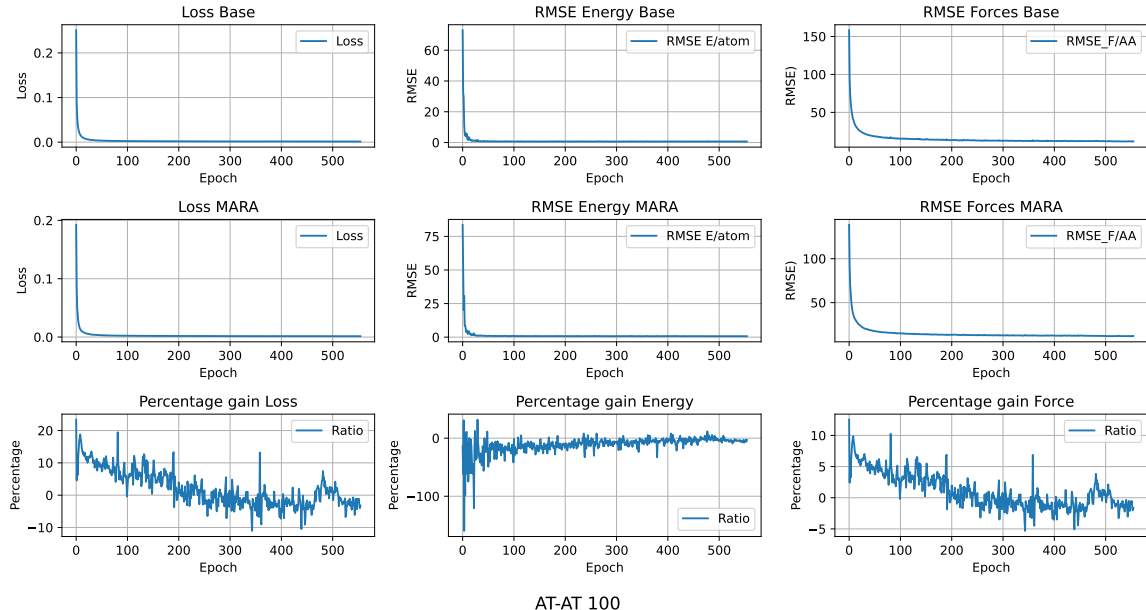


Figure 8. Performance of models on the validation set on AT-AT with 100 samples. The subplots show, from left to right, Loss, Energy, and Strength; from top to bottom, Baseline, MARA, and the percentage ratio.

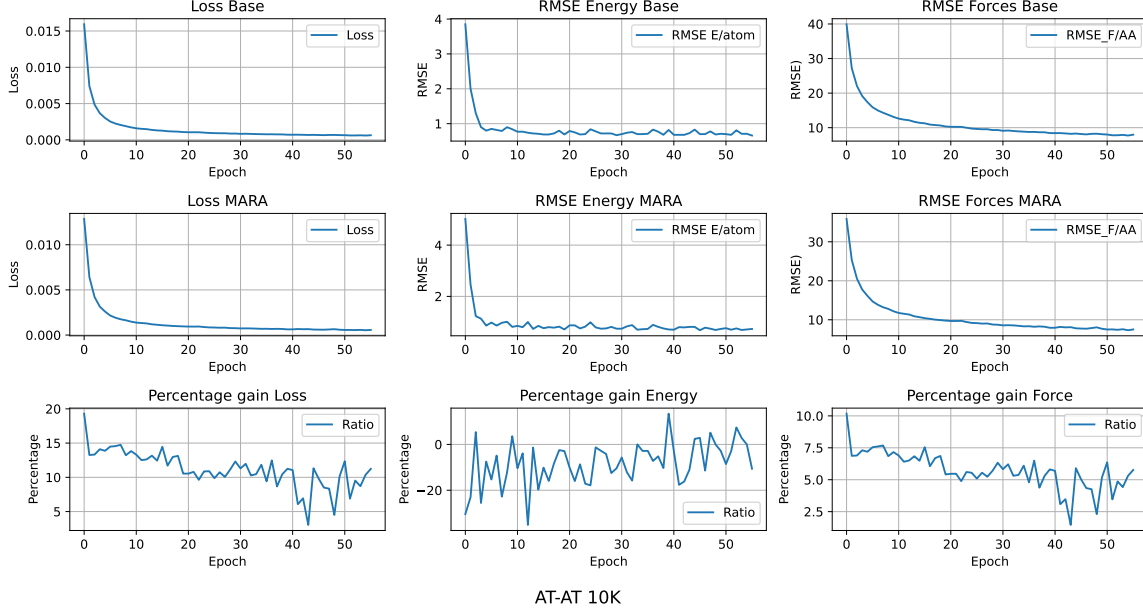


Figure 9. Performance of models on the validation set on AT-AT with 10,000 samples. The subplots show, from left to right, Loss, Energy, and Strength; from top to bottom, Baseline, MARA, and the percentage ratio.

Figures 8 and 9 show that, for AT-AT pairs, MACE-MARA yields worse force predictions than the baseline when trained on 100 samples, while outperforming it in the 10k-sample regime. In both settings, the module initially underperforms the baseline; however, with 100 samples, despite a substantial improvement in energy prediction during training, the performance ratio never becomes positive. In contrast, with 10,000 samples, training enables MACE-MARA to match the baseline performance on energies.

Regarding forces, an opposite trend is observed. MACE-MARA starts with a positive ratio, which decreases sharply in the 100-sample regime, whereas it remains more stable when trained on 10,000 samples. This behavior results in degraded test-set performance in the low-data regime and a clear overall improvement when sufficient training data are available.

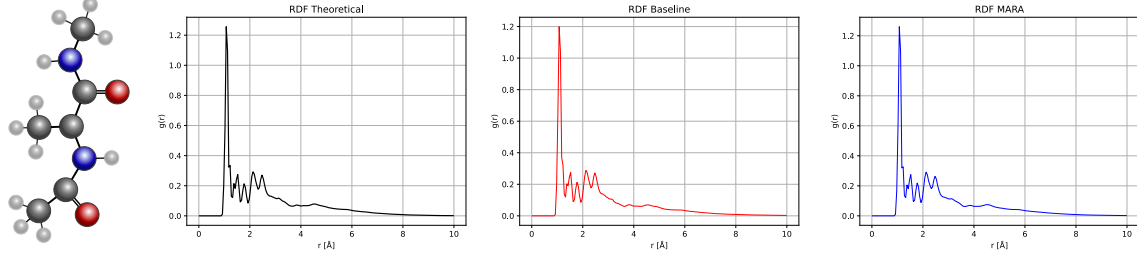
E. Performance analysis during molecular dynamics

To verify that the introduced module remains useful for molecular dynamics (MD) prediction and does not compromise the stability of the base model, we perform a short MD simulation using the Atomic Simulation Environment (ASE) framework (Bahn & Jacobsen, 2002; Larsen et al., 2017). The test system is the capped peptide Ac-Ala₃-NHMe. Initial velocities are sampled from the Maxwell–Boltzmann distribution at 500 K, and the simulation runs in the NVT ensemble using a Langevin thermostat with a friction coefficient of 0.1. The integration time step is 1 fs, and the trajectory is propagated for 10 000 fs (10 ps).

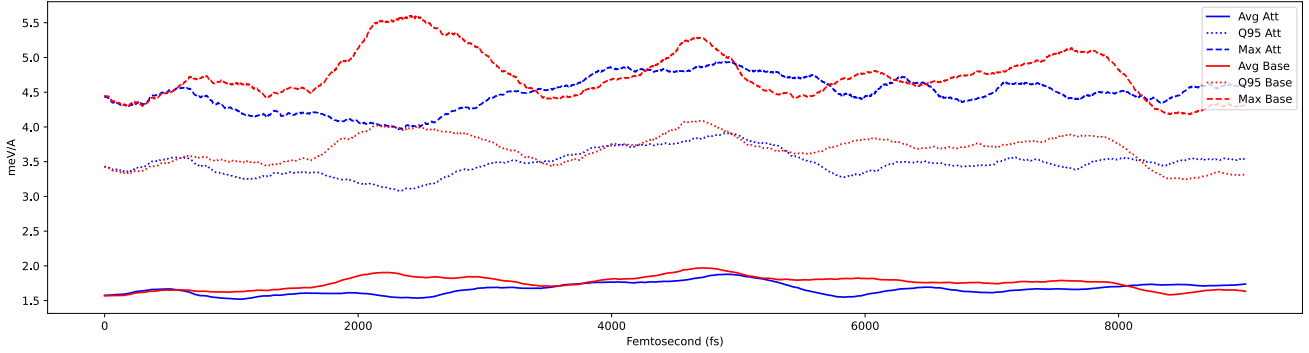
In Figure 10a, we compare the radial distribution function (RDF) computed from the MD22 reference dataset with the RDF obtained from the 10 000 configurations generated during the simulation, for both MACE and MACE-MARA.

In Figure 10b, we report the evolution of the force magnitude acting on the atoms: at each time step we compute the mean, the 95th percentile, and the maximum norm of the force. Since per-step measurements are highly noisy, we apply a 500 fs moving average window to highlight the overall trend.

Both models reproduce an RDF that is consistent with the reference RDF (MD22), indicating that the introduced module does not significantly distort the structural distribution. From Figure 10b, the force trajectories of the two models largely overlap and no divergence or numerical instability is observed. Moreover, fluctuations in MACE-MARA are slightly reduced compared to the baseline MACE model, suggesting that the attention mechanism may act as an adaptive filter, in agreement



(a) Radial distribution function (RDF) computed from the MD22 reference dataset, on MACE and MARA computed on MD simulations



(b) Molecular dynamics on Ac-Ala₃-NHMe

Figure 10. MD validation. (a) RDF comparison of MACE and MACE-MARA with the MD22 reference. (b) Force magnitude statistics (mean, 95th percentile, maximum) during a 10 ps MD run on Ac-Ala₃-NHMe (1 fs timestep, NVT Langevin at 500 K, moving average window 500 fs).

with observations reported in previous works (Veličković et al., 2018; Brody et al., 2022).

Finally, the computational overhead introduced by the module is small: on an NVIDIA H100 GPU, the simulation with MACE ($\ell = 2$, grid resolution 4×8) takes 940 s, while MACE-MARA requires 1007 s, corresponding to an overhead of approximately 7.1% (about half of the cost reported in Table 4). This additional validation suggests that the proposed spherical attention mechanism, when integrated into a state-of-the-art SE(3)-equivariant model such as MACE, still allows for realistic MD simulations.

F. Plug and play in other models

As noted in the main text, our model is plug-and-play and can be integrated into SE(3)-equivariant architectures without significant structural modifications, enabling rapid adoption. In the main text, we employ MACE (Batazia et al., 2022b), a body-ordered tensor network widely used in molecular dynamics. However, this choice does not restrict the applicability of MARA to MACE-based models.

In this appendix, we demonstrate the integration of MARA into other SE(3)-equivariant frameworks. Specifically, we implement MARA within NequIP (Batzner et al., 2021), which is a message-passing architecture operating on irreducible representations. We use the original NequIP framework (<https://github.com/mir-group/nequip>) and report results on the aspirin molecule from the MD17 dataset (Chmiela et al., 2017). Finally, we apply MARA to the attention-based equivariant model VisNET (Wang et al., 2024), evaluating performance on the aspirin molecule from the MD17 dataset, further demonstrating the generality of the proposed approach across diverse equivariant architectures.

F.1. NequIP

As done in MACE, MARA is inserted into the InteractionBlock. For the test, we set the cutoff radius to 5.0 Å. The NequIPGNModel is configured with a Bessel encoding of 8 basis functions, which are not trainable, and a polynomial cutoff exponent of 6. The convolutional network comprises 3 interaction layers, with $\ell_{\max} = 1$, parity enabled, and 32

features per node. The radial network consists of 2 layers with 64 hidden units each. Dataset statistics are used to normalize the model, including the average number of neighbors, per-type energy scales based on force RMS, and per-type energy shifts based on per-atom energy mean.

Table 8. Analyzing the performance of NequIP and NequIP-MARA on Aspirin from MD17 dataset.

METRIC	NEQUIP	NEQUIP-MARA	$\Delta(\%)$
FORCES MAE	0.0558	0.0499	-10.57
FORCES MAX ERROR	1.0779	0.8810	-18.27
FORCES RMSE	0.0760	0.0682	-10.26
ATOM MAE	0.0018	0.0012	-33.33
ATOM MAX ERROR	0.0155	0.0121	-21.94
ATOM RMSE	0.0022	0.0016	-27.27
TOTAL ENERGY MAE	0.0391	0.0269	-31.20
TOTAL ENERGY MAX ERROR	0.3268	0.2542	-22.22
TOTAL ENERGY RMSE	0.0478	0.0342	-28.45
WEIGHTED SUM	0.0475	0.0384	-19.16

Analyzing the performance, we observe that MARA consistently improves NequIP on Aspirin from the MD17 dataset. Table 8 reports the results obtained on the test set at the end of training. In this case, the gains are considerably larger than those observed for MACE, which may result from suboptimal NequIP settings, whereas in the main text we used a highly expressive MACE model. Nevertheless, it is evident that MARA provides a substantial improvement even on a model different from MACE.

Algorithm 2 Forward pass of NequIP

```

1:  $x \leftarrow \text{linear\_1}(x)$ 
2: normalize  $x$  via avg_num_neighbors
3: if not first layer then
4:    $x \leftarrow \text{ghost\_exchange}(x)$ 
5: end if
6:  $x, att \leftarrow \text{MARA}(x, positions, edge\_index)$ 
7:  $x \leftarrow \text{tp\_scatter}(x, edge\_attrs, edge\_weights, edge\_src, edge\_dst)$ 
8:  $x \leftarrow \text{linear\_2}(x)$ 
9:  $data[\text{NODE\_FEATURES\_KEY}] \leftarrow x$ 

```

F.2. VisNET

To insert MARA into VisNET (<https://github.com/ElwynWang/ViSNet/tree/main>), it is necessary to adjust ViSNetBlock and the related Message Passing (ViS MP). Node features are embedded into a latent space of dimension 256 and processed through 5 stacked VisNET blocks, each incorporating spherical harmonics up to order $\ell_{max}=2$. Radial interactions are modeled using 32 exponential-normalized radial basis functions with a cutoff radius of 5.0 Å. The attention mechanism uses 8 heads with SiLU activations and aggregates messages via summation. VisNET is trained using a combined energy–force loss, with forces dominating the objective, reflecting standard practice in molecular dynamics learning.

Table 9. Analyzing the performance of VisNET and VisNET-MARA on Aspirin from MD17 dataset.

METRIC	VISNET	VISNET-MARA	$\Delta(\%)$
SCALAR MAE	0.1850	0.1369	-26.00
FORCES MAE	0.1679	0.1645	-2.03

Table 9 shows that the results on the aspirin test set from the MD17 data set demonstrate that MARA produces a significant performance improvement also in attention-based equivariant models.

We introduce the model as illustrated in pseudocode 3, treating MARA as a separate modular unit, and report the corresponding results in Table 9. We note that an alternative and equally natural integration of MARA within VisNET is shown in pseudocode 4.

Algorithm 3 Forward pass of VisNET block with MARA-style attention

```

1:  $x \leftarrow \text{LayerNorm}(x)$ 
2:  $x, att \leftarrow \text{MARA}(x, \text{pos}_{ij}, \text{edge\_index})$ 
3:  $q \leftarrow \text{Linear}_q(x)$ 
4:  $k \leftarrow \text{Linear}_k(x)$ 
5:  $v \leftarrow \text{Linear}_v(x)$ 
6:  $d_k \leftarrow \sigma(\text{Linear}_{dk}(f_{ij}))$ 
7:  $d_v \leftarrow \sigma(\text{Linear}_{dv}(f_{ij}))$ 

```

Algorithm 4 Message function of VisNET block with MARA-style attention

```

1:  $a_{ij} \leftarrow \sum(q_i \odot k_j \odot d_k)$ 
2:  $a_{ij} \leftarrow \sigma_{\text{attn}}(a_{ij}) \cdot \text{cutoff}(r_{ij})$ 
3:  $v_j \leftarrow v_j \odot d_v$ 
4:  $v_j \leftarrow v_j \odot a_{ij}$ 
5:  $v_j, att_{\text{MARA}} \leftarrow \text{MARA}(v_j, \text{pos}_{ij}, \text{edge\_index})$ 
6:  $(s_1, s_2) \leftarrow \text{Split}(\sigma(\text{Linear}_s(v_j)))$ 

```
